An Enhanced Axisymmetric Solid Element for Rotor Dynamic Model Improvement

Lingnan Hu[1]
Mem. ASME
Department of Mechanical Engineering,
Texas A&M University,
3123 TAMU,
College Station, TX 77843
e-mail: lingnan@tamu.edu

Alan Palazzolo
James J. Cain Professor
Fellow ASME
Department of Mechanical Engineering,
Texas A&M University,
3123 TAMU,
College Station, TX 77843
e-mail: a-palazzolo@tamu.edu

The authors present an improved formulation for the axisymmetric solid harmonic finite element (FE) modeling of a flexible, spinning rotor. A thorough comparison of beam-type FE and axisymmetric solid FE rotor models is presented, indicating the errors that result from beam FE usage for various nondimensional rotor topologies. The axisymmetric rotor is meshed in only two dimensions: axial and radial, with both displacement fields being represented with Fourier series expansions. Centrifugal stress-stiffening and spin-softening effects are included in all elements and most importantly in modeling flexible disks. Beam FE and axisymmetric FE natural frequencies, mode shapes, and critical speeds are compared to identify shaft geometries where the beam model yields a significant error. Finally, limitations of beam FE models and guidance for utilizing axisymmetric solid FE models in rotor dynamic simulations are provided. [DOI: 10.1115/1.4043411]

Introduction

Accurate prediction of resonant speeds and instability in rotating machinery has long been an important concern for designers of turbomachinery. Historically, multistation rotors were originally modeled with transfer matrix methods [1,2]. This approach has been for the most part replaced with the use of the finite element method due to the increased speed of computers and the development of highly efficient algorithms for solving finite element (FE) equations. FE modeling approaches for rotor dynamic response have used both Euler–Bernoulli and Timoshenko beam elements. Nelson and McVaugh [3] developed a general cylindrical rotating shaft model using beam elements and including gyroscopic effects, rotary inertia, and axial loads. This was subsequently extended by Nelson [4] to include shear deformation and torque effects. Thomas et al. [5] considered conical shaft sections and utilized two additional coordinates at the element ends to improve the modeling of shear deformation. On the basis of their work, Rouch and Kao [6] developed linearly tapered beam elements by applying numerical integration to derive element matrices. In order to use closed-form expressions rather than numerical integration, Greenhill et al. [7] employed the kinematic representation of the beam FE model in Ref. [5] and derived closed-form polynomial expressions for element matrices. A shear deflection factor is employed in their work to assess the effect of cross-sectional shape on shear deformation.

The basic beam assumption that plane sections remain plane after deformation is made for the beam element formulation in this work. The deformations that violate this assumption are considered as non-beam deformations. In most cases, shafts have small bending displacements compared with the length, and the plane sections after deformation may be approximated to be plane. Hence, it has been generally believed that the aforementioned beam FE models are able to yield acceptable results. However, a rising number of shafts with complex shapes are designed for modern turbomachinery, and as such, the beam assumption may be violated at sections with large diameter changes, which has been verified by Stephenson et al. [8]. Besides, a shaft that is composed of hollow conical segments may not be precisely modeled with beam elements due to distortions occurring at the hollow conical sections. Vest and Darlow

[9] came up with correction factors to include the effect of distortions on the beam stiffness. However, this approach is limited to certain cases and is unable to precisely predict the full range of natural frequencies.

An alternative approach, which is different than applying various correction factors to beam FE formulations, has been developed by Stephenson and Rouch [10]. They utilized two-and-one-half-dimensional (2.5D) solid harmonic elements to model axisymmetric shafts and extended the formulations to include the gyroscopic effects based on the work of Cook et al. [11] and Geradin and Kill [12]. Genta and Tonoli developed one-and-one-half-dimensional (1.5D) axisymmetric element models for flexible thin disks and blades [13,14], which account for gyroscopics, centrifugal, and thermoelastic loadings. Their disk 1.5D axisymmetric FE model is reduced to its midplane and has two displacement coordinates, radial and polar angle displacements. Greenhill and Lease [15] investigated the influences of disk flexibility and locations on the rotor system by using axisymmetric solid harmonic elements, but they did not consider the centrifugal stress-stiffening and spin-softening effects. Genta presented an improved 2.5D axisymmetric element model for an axisymmetric rotor [16]. Although centrifugal and thermal loading are considered in their rotor FE model, detailed FE matrices and formulations are not provided.

Axisymmetric element rotor models may be more efficient, but their limitations are recognized when a nonaxisymmetric rotor model is required. Genta presented a modal approach [17] for 1D or 1.5D nonaxisymmetric beam-type rotor modeling, which can be extended to three-dimensional (3D) modeling. In addition, Genta proposed a general-purpose 3D FE modeling approach [16] for non-axisymmetric rotors assuming small deflections, and that a single spin axis exists for each point of the rotating structure. Datta [18] presented an approach that solves the 3D governing equations and includes aeromechanics stress and strain solutions for trim and transient conditions. In regard to a rotor system with stationary parts like housings, Tseng et al. [19] used solid elements to discretize the axisymmetric rotor and the housing having arbitrary geometry in the rotor- and ground-based coordinate systems, respectively. Kiesel and Marburg [20] used 3D FE models in ABAQUS to simulate a complex nonlinear rotor system and show that 3D rotor modeling and analysis can be done with a commercial general-purpose FE code. With regard to support boundary conditions, Stephenson and Rouch [10] mentioned that it is reasonable to apply bearing stiffness and damping to the outer surface node of a shaft, but they neither specified how to include these coefficients in the shaft matrices nor validated this point of view.

Hu and Palazzolo [21] used a rigid and massless beam web with a fictitious node, which is centered at the web and connected to the surrounding nodes, to attach the bearing stiffness and damping to the shaft model.

As disks in the modern design of some high-speed turbomachines are becoming thinner and more flexible, additional attention may be required for both centrifugal stress-stiffening and spin-softening effects. Cook et al. [11] derived equations in the Cartesian coordinate system to interpret initial stress phenomena. However, their method cannot be directly applied in the axisymmetric FE rotor model on account of rotor rotation and the different definition of the Cartesian and cylindrical coordinate systems. The centrifugal stress-stiffening and spin-softening effects have not been adequately addressed in the rotor dynamics literature. Combescure and Lazarus [22] provided an axisymmetric FE model in the rotating frame to study the centrifugal stress-stiffening effects. Although they presented a general equation of motion including the centrifugal stress-stiffening and spin-softening effects, they did not provide detailed FE matrices and a procedure to implement their formulation. In addition, their axisymmetric FE model is in the rotating frame, which has limited applications.

This paper presents an improved axisymmetric solid FE formulation of the centrifugal stress-stiffening and spin-softening effects, which is applicable in rotor dynamic modeling and analysis. In addition, the paper investigates the individual influences of either thin-walled shafts or flexible disks and the combined influences of both shafts and disks on the rotor system. A discussion and guidance are provided on a proper attachment of the bearing stiffness and damping to a thin-walled shaft mode. Various combinations of thin-walled shafts and flexible disks are modeled, and the influences of the flexibility of the shaft and disk on the accuracy of the resonance prediction are investigated. The conclusions drawn from the simulation results and analyses may provide designers and engineers with guidelines on when and how to use an axisymmetric FE model instead of a beam FE model for rotor dynamic analysis.

Axisymmetric Element Modeling of Rotor

Extreme performance and efficiency requirements have caused modern rotor designs to become lighter-weight and operate at increasingly higher speeds. This may require shafts to have complex thin-wall and thin-disk designs and to operate through more resonant speeds. These evolving requirements may not be adequately met by beam FE models and instead require more general solid FE models.

The axisymmetric element model is a good replacement of the beam element model for rotor dynamic modeling. In general, the axisymmetric element is one type of solid elements that can fill a 3D space. The only limitation is that the 3D space must be axisymmetric. Shaft warping and flexural disk modes, which cannot be modeled with beam elements due to a violation of the beam assumption, can be modeled using axisymmetric elements. This yields higher accuracy than not including effects of shaft warping and flexural disk modes for rotor dynamic response prediction. Including those effects removes kinematic assumptions imposed on the deformation field, which will improve the modeling fidelity. The present paper provides theoretical development and numerical examples for an extended axisymmetric solid harmonic element especially useful for high-fidelity modeling of flexible rotors with shafts, disks, and general bearings.

Theory. A 3D axisymmetric structure can be formed by rotating the longitudinal semisection plane about the axis of symmetry. Furthermore, the rotor displacements of the longitudinal semisection plane can be expanded circumferentially using the Fourier series in the angle taken about the axis of symmetry. That being said, a two-dimensional (2D) plane mesh filled with axisymmetric elements can represent a 3D rotor. More details are given in Refs. [11,23].

In the present work, the longitudinal semi-section region of a rotor is filled with linear triangle elements in order to cover irregularly shaped areas. Just to clarify, the methodology of the axisymmetric FE formulation presented here is applicable not only to the triangle element type but also to other axisymmetric element types. As shown in Fig. 1, the shaded area with nodes 1, 2, and 3 represents the three-node triangle element. The displacements of each element are attained through the superposition of both symmetric and antisymmetric components at all harmonics, which may be expressed as

$$\{\mathbf{U_R^e}\} = \begin{bmatrix} u_r \\ u_z \\ u_\theta \end{bmatrix} = \begin{bmatrix} \sum_{m=0}^{\infty} (U_{mrS}\cos(m\theta) + U_{mrA}\sin(m\theta)) \\ \sum_{m=0}^{\infty} (U_{mzS}\cos(m\theta) + U_{mzA}\sin(m\theta)) \\ \sum_{m=0}^{\infty} (U_{m\theta S}\sin(m\theta) - U_{m\theta A}\cos(m\theta)) \end{bmatrix} \quad (1)$$

where u_r, u_z, and u_θ represent the radial, axial, and circumferential displacements, respectively. U_{mij} with $i = r, z, \theta$ representing the radial, axial, or circumferential displacement component and $j = S, A$ representing the symmetric or antisymmetric displacement component is the node degree-of-freedom (DOF) of an element for the mth harmonics. Then element displacements $\{\mathbf{U_R^e}\}$ can be further approximated by

$$\{\mathbf{U_R^e}\} = [\mathbf{N}]\{\mathbf{q^e}\} \quad (2)$$

where the node DOF vector of the element $\{\mathbf{q^e}\}$ and the corresponding shape function $[\mathbf{N}]$ can be found in Refs. [10,15].

The harmonics of interest in this work are $m = 0, 1, 2$. The zeroth-order harmonics contribute to a radial expansion u_0, an axial displacement v_0, and a torsional rotation w_0. Both first- and second-order harmonics describe the displacements in the YZ plane and the rotations about the X axis of the finite element. Below are the two reasons to set $m = 0, 1, 2$. First, extensive numerical tests have shown that including higher harmonics, above 2, significantly increases computation time, but yields little in terms of increased accuracy of rotor dynamic analysis [8,11,24]. Second, although the first-order harmonics are the only harmonics of interest for a shaft in purely lateral bending scenarios [8,15], this may be insufficient in the case of thin-walled shafts as thin-walled structures are prone to warping. A flexible disk may have local flexural modes below the critical speeds, which requires an axisymmetric FE model with higher harmonics. Therefore, the second-order harmonics representing the local modes that are uncoupled from the lateral modes of the shaft are employed. In addition, the zeroth-order harmonics are included in order to account for the centrifugal stress-stiffening effects.
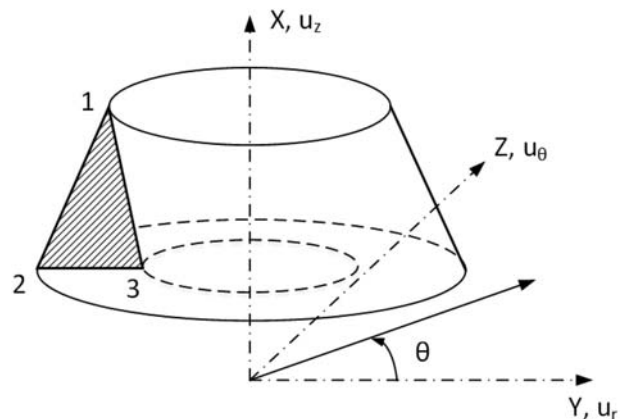

Fig. 1 Solid of revolution generated from a linear axisymmetric triangle element

The axisymmetric FE rotor model can be obtained by assembling the equations of motion of all elements. The equation of motion for an individual axisymmetric element may be expressed as

$$[\mathbf{M_R^e}]\{\ddot{\mathbf{U}}_\mathbf{R}^\mathbf{e}\} + [\mathbf{C_R^e}]\{\dot{\mathbf{U}}_\mathbf{R}^\mathbf{e}\} + [\mathbf{K_R^e}]\{\mathbf{U_R^e}\} = \{\mathbf{f_R^e}\} \qquad (3)$$

where $[\mathbf{M_R^e}]$, $[\mathbf{C_R^e}]$, and $[\mathbf{K_R^e}]$ represent the total mass, damping, and stiffness matrices of the rotor element, respectively. $\{\mathbf{f_R^e}\}$ is the external force vector. $\{\mathbf{U_R^e}\}$ is obtained by assembling the displacements at all harmonics.

In regard to Eq. (3), the total damping matrix $[\mathbf{C_R^e}]$ contains gyroscopic matrix and viscous structural damping matrix (negligible effect for most rotors). The total stiffness matrix $[\mathbf{K_R^e}]$ contains the elastic stiffness, centrifugal stress-stiffening, and spin-softening matrices. $\{\mathbf{f_R^e}\}$ contains unbalanced forces and bearing forces. The damping and stiffness matrices derived from bearing forces will be integrated into $[\mathbf{C_R^e}]$ and $[\mathbf{K_R^e}]$, respectively. The formulations of the mass, gyroscopic, and elastic stiffness matrices have been provided in Refs. [8,15]. However, other important contributions to the rotating system element matrices were not included in those references, such as bearing forces, centrifugal stress-stiffening, and spin-softening. These matrices will be derived and presented here.

Bearing Attachment. One of the key factors that affect the prediction of critical speeds is the approach of attaching linear force coefficients of transient bearing forces to the shaft model. Bearing coefficients or forces are connected at a node corresponding to the bearing centerline in a shaft beam FE model, regardless of whether the shaft is solid or hollow. In contrast, there are many nodes at the bearing centerline position in an axisymmetric FE model, but none on the shaft axis if the shaft is hollow. One approach is to connect the bearing coefficients or force to a single surface node of the journal. However, this may be inadequate for a thin-walled shaft that may distort locally or a bearing with a large longitudinal length. Therefore, an improved approach is presented in Fig. 2.

The damping and stiffness dynamic force coefficients of fluid film bearings and seals are generally measured or obtained by numerically solving Reynold's equation for pressure and integrating to obtain force. The Y and Z reaction forces exerted by the bearing on the journal are represented by the general linearized forces

$$\begin{aligned}
F_y &= -K_{yy}w_y - K_{yz}w_z - C_{yy}\dot{w}_y - C_{yz}\dot{w}_z \\
F_z &= -K_{zy}w_y - K_{zz}w_z - C_{zy}\dot{w}_y - C_{zz}\dot{w}_z
\end{aligned} \qquad (4)$$

where $w_y, w_z, \dot{w}_y, \dot{w}_z$ represent the Y and Z transverse displacements, and Y and Z velocities at the bearing centerline and at the center of the shaft, respectively. The challenge is how to "distribute" the dynamic coefficients, $K_{yy}, K_{yz}, K_{zy}, K_{zz}$ (also called linear stiffness coefficients) and $C_{yy}, C_{yz}, C_{zy}, C_{zz}$ (also called linear damping coefficients) over the axisymmetric FE journal surface nodes in a manner that yields the same forces as defined in Eq. (4). The following procedure and analysis are employed to fit the dynamic coefficients of a bearing in the rotor axisymmetric FE model.

As can be seen from Fig. 3, the bearing forces F_y and F_z, which act on node P, translate from the cylindrical coordinates to the Cartesian coordinates as

$$\begin{aligned}
w_y^P &= u_r^P\cos(\theta) - u_\theta^P\sin(\theta) \\
w_z^P &= u_r^P\sin(\theta) + u_\theta^P\cos(\theta)
\end{aligned} \qquad (5)$$

where the superscript represents node P. u_r^P, u_θ^P are scalar displacements of node P corresponding to the unit vectors $\mathbf{e_r}, \mathbf{e_\theta}$ in the cylindrical coordinates, respectively. u_r^P and u_θ^P can be decomposed into different harmonics by using Fourier series, which is similar to Eq. (1).

Before applying stiffness and damping coefficients of a linear bearing model to an axisymmetric FE rotor, three prerequisites are clarified as follows. First of all, bearing forces act on the outer circumferential surface of a journal. Second, most rotating machines operate far below the critical speed for the local journal deformation modes. This factor leads to a practically appropriate assumption that the node circumferential circle at P may be assumed a rigid node circle moving with a constant displacement for all the nodes on the circle (also called rigid node circle). Finally, the expansion or shrink of the journal is generally negligible in comparison with lateral displacements caused by shaft bending. However, there are a few thermal expansion cases in which the expanding journal may have an impact on the rotor stability [25,26]. Accordingly, an asymmetric journal model and probably transient analysis are required to investigate those minority cases. Based on the above three prerequisites, the first-order harmonics, which contribute to the lateral displacement, are used to approximate the total displacement of node P in the cylindrical coordinates u_r^P and u_θ^P as

$$\begin{aligned}
u_r^P &= U_{1rS}^P\cos(\theta) + U_{1rA}^P\sin(\theta) \\
u_\theta^P &= U_{1\theta S}^P\sin(\theta) - U_{1\theta A}^P\cos(\theta)
\end{aligned} \qquad (6)$$

Substituting Eq. (6) into Eq. (5) yields

$$\begin{aligned}
w_y^P &= U_{1rS}^P\cos^2(\theta) - U_{1\theta S}^P\sin^2(\theta) + (U_{1rA}^P + U_{1\theta A}^P)\sin(\theta)\cos(\theta) \\
w_z^P &= U_{1rA}^P\sin^2(\theta) - U_{1\theta A}^P\cos^2(\theta) + (U_{1rS}^P + U_{1\theta S}^P)\sin(\theta)\cos(\theta)
\end{aligned} \qquad (7)$$

Per the rigid node circle assumption, the lateral displacements w_y and w_z are constant for all nodes (i.e., all θ) on the rigid circle. This implies that w_y and w_z shown in Eq. (7) are constant regardless of θ.
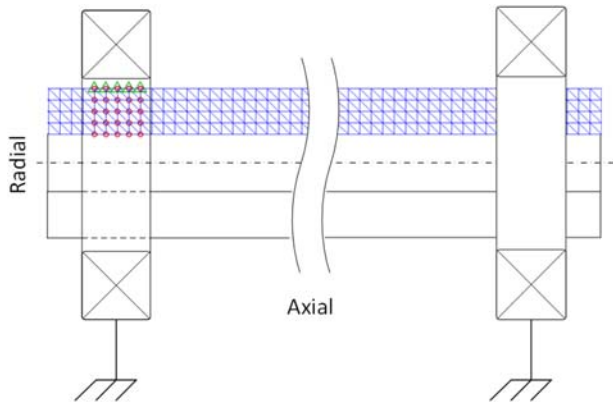

Fig. 2   Mesh model of a hollow shaft supported by two bearings: triangles represent the surface nodes to which the bearing forces are distributed and circles denote the nodes of the stiffened elements
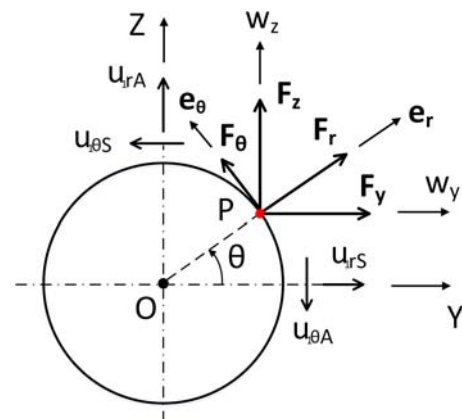

Fig. 3   Bearing forces on the node of an axisymmetric element

As a result, the relationship between displacement components can be obtained as

$$U_{1\theta S}^P = -U_{1rS}^P$$
$$U_{1\theta A}^P = -U_{1rA}^P$$

(8)

The bearing force acting on node P is expressed as

$$dF_y^P = \frac{K_{yy}w_y^P + K_{yz}w_z^P}{2\pi}d\theta$$
$$dF_z^P = \frac{K_{zy}w_y^P + K_{zz}w_z^P}{2\pi}d\theta$$

(9)

As shown in Fig. 3, the bearing forces F_y and F_z translate from Cartesian coordinates to the cylindrical coordinates. Then, applying the forces circumferentially to the rigid circle yields the resultant generalized force Q_j^P as

$$Q_j^P = \int_0^{2\pi} dF_r^P \vec{e}_r \cdot \frac{\partial u_r^P}{\partial q_j} \vec{e}_r + \int_0^{2\pi} dF_\theta^P \vec{e}_\theta \cdot \frac{\partial u_\theta^P}{\partial q_j} \vec{e}_\theta$$

(10)

where $\vec{e}_r$, $\vec{e}_\theta$ (equivalent to bold $\mathbf{e_r}$, $\mathbf{e_\theta}$ shown in Fig. 3) represent unit vectors in the radial and tangential directions, respectively. The terms dF_r^P and dF_θ^P represent the differential bearing forces in the radial and circumferential directions, respectively, where both dF_r^P and dF_θ^P are scalars. The generalized bearing force Q_j^P, which corresponds to the jth DOF q_j, contains bearing stiffness coefficients and displacement DOF terms. Substituting Eqs. (1), (7), (8), and (9) in Eq. (10) yields Q_j^P, the formulation of which is detailed in the Appendix. The bearing stiffness coefficients are integrated into $[\mathbf{K_R^e}]$ by adding Q_j^P into $\{\mathbf{f_R^e}\}$ of Eq. (3) and rearranging the DOF-related terms. The damping coefficients of the bearing can be obtained by simply replacing the stiffness coefficients K with C as the derivation for the damping coefficients follows the same path as the stiffness coefficients.

As depicted in Fig. 4, the stiffness coefficients K_{yy}, K_{yz}, K_{zy}, K_{zz} and the damping coefficients C_{yy}, C_{yz}, C_{zy}, C_{zz} of a bearing are equally divided by five, which equals the number of surface nodes, and are added to each surface node on the journal. Bearing lubricant-induced forces occur on the longitudinal length of the shaft inside the bearing, which is also called the journal. The bearing forces are assumed to be equally distributed (the distribution proportion is adjustable) on the surface nodes of the journal in the axisymmetric element model. A thin-walled journal model may also be artificially stiffened (an increase in modulus of

elasticity of the element nodes represented by circles shown in Fig. 4) for certain types of bearings. The degree of artificial stiffening can be varied by the analyst to balance excessive journal deformation versus the increased numerical integration time that may result from artificial stiffening [24] (Sec. 4.8.17 in Ref. [24]).

The bearing forces are applied to the journal in a distributed manner because applying the forces or linearized force coefficients (stiffness, damping, inertia) at a single node may result in excessive local deformation at the point of application especially when the journal is thin walled and the bearing forces or dynamic coefficients are large. The simulation results will later illustrate this by an example.

Centrifugal Stress-Stiffening. Centrifugal stress-stiffening may have a significant effect on rotor dynamic response especially at high spin rates and for highly flexible disks and shafts. Consider a rotating shaft-disk system. The disk is radially under tensile load due to the centrifugal forces, which creates a restoring force for axial deflection and hence raises the disk's bending stiffness and natural frequencies for disk flexural and axial modes. As the tensile load causes radial strain expansion, only the component of the zeroth-order harmonics is associated with the centrifugal stress-stiffening.

To include the centrifugal stress-stiffening effects, an improved formulation of the axisymmetric FE rotor model in the cylindrical coordinate system is presented in this section, as an extension to Cook et al.'s work [11]. The centrifugal forces cause the initial strain ε_0 and the initial stress σ_0 prior to the bending of the rotor, as shown in Fig. 5.

As the rotor has further deformations on the basis of the initial strain, the strain energy U that excludes the elastic potential energy caused by centrifugal forces prior to rotor bending consists of two parts: one caused by centrifugal forces (represented by the shaded area in Fig. 5) and the other resulting from rotor displacement (represented by the blank area in Fig. 5). The strain energy of the spinning rotor when bending U may be expressed as

$$U = \frac{1}{2}\int_V \{\boldsymbol{\varepsilon}\}^T\{\boldsymbol{\sigma}\}dV + \int_V \{\boldsymbol{\varepsilon}\}^T\{\boldsymbol{\sigma_0}\}dV$$

(11)

where the first and second components represent the two parts of the elastic potential energy shown in Fig. 5, respectively. The terms $\{\boldsymbol{\sigma}\}$ and $\{\boldsymbol{\varepsilon}\}$ are vectors containing the component stresses and strains, which exclude the initial stress and strain. The term $\{\boldsymbol{\sigma_0}\}$ is a vector containing the initial stresses induced only by centrifugal force.

The linear small strain (also called infinitesimal strain) model, which is widely used in engineering (including rotor dynamics), may not be an appropriate model for rotors with highly flexible disks or blades. This is because the small rotation assumption for the small strain model may be violated when the amount of rotation (such as for bending of a flexible disk) becomes large. A remedy is to employ the Green strain model in mechanics with the tensorial strain, $\tilde{\varepsilon}$. Only the second-order terms of $\tilde{\varepsilon}$ are related to the centrifugal force-induced strains in rotor bending [11]. Replacing tensor-
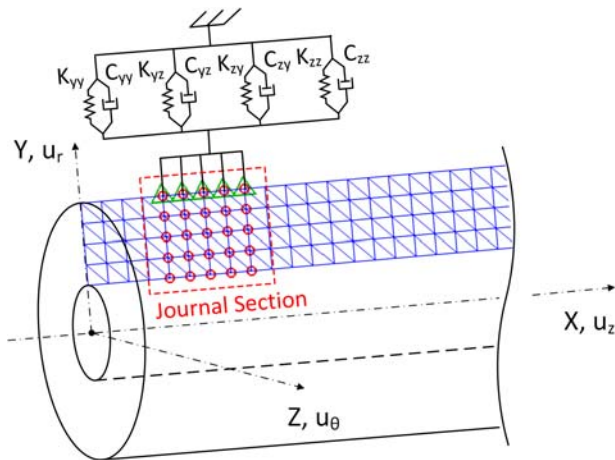

Fig. 4 Add stiffness and damping coefficients of a bearing to the nodes in the longitudinal semi-section of a shaft: triangles and circles represent the surface nodes and the stiffened element nodes, respectively
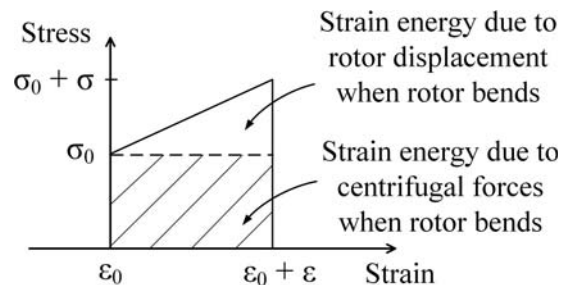

Fig. 5 Strain energy due to centrifugal forces and vibration

based shear terms in $\tilde{\varepsilon}$ with engineering shear strains yields the second-order strains as

$$\varepsilon_{2r} = \frac{1}{2}\left[\left(\frac{\partial u_r}{\partial r}\right)^2 + \left(\frac{\partial u_z}{\partial r}\right)^2 + \left(\frac{\partial u_\theta}{\partial r}\right)^2\right]$$

$$\varepsilon_{2z} = \frac{1}{2}\left[\left(\frac{\partial u_r}{\partial z}\right)^2 + \left(\frac{\partial u_z}{\partial z}\right)^2 + \left(\frac{\partial u_\theta}{\partial z}\right)^2\right]$$

$$\varepsilon_{2\theta} = \frac{1}{2r^2}\left[\left(u_r + \frac{\partial u_\theta}{\partial \theta}\right)^2 + \left(u_\theta - \frac{\partial u_r}{\partial \theta}\right)^2 + \left(\frac{\partial u_z}{\partial \theta}\right)^2\right]$$

$$\gamma_{2rz} = \frac{\partial u_r}{\partial r}\frac{\partial u_r}{\partial z} + \frac{\partial u_z}{\partial r}\frac{\partial u_z}{\partial z} + \frac{\partial u_\theta}{\partial r}\frac{\partial u_\theta}{\partial z}$$

$$\gamma_{2z\theta} = \frac{1}{r}\left[\frac{\partial u_\theta}{\partial z}\left(u_r + \frac{\partial u_\theta}{\partial \theta}\right) + \frac{\partial u_r}{\partial z}\left(-u_\theta + \frac{\partial u_r}{\partial \theta}\right) + \frac{\partial u_z}{\partial z}\frac{\partial u_z}{\partial \theta}\right]$$

$$\gamma_{2r\theta} = \frac{1}{r}\left[\frac{\partial u_\theta}{\partial r}\left(u_r + \frac{\partial u_\theta}{\partial \theta}\right) + \frac{\partial u_r}{\partial r}\left(-u_\theta + \frac{\partial u_r}{\partial \theta}\right) + \frac{\partial u_z}{\partial r}\frac{\partial u_z}{\partial \theta}\right]$$

(12)

where the subscript 2 indicates the second-order strains.

The strain energy due to the bending of the rotor that undergoes centrifugal forces may be expressed as

$$U_\sigma^e = \int_{V^e} \{\varepsilon_2^e\}^T \{\sigma_0^e\} dV \tag{13}$$

The elastic potential energy shown in Eq. (13) is derived from Eq. (11) by excluding the first-order strain terms.

The generalized force representing the centrifugal forces and corresponding to the jth node DOF may be expressed as

$$Q_{Vj}^e = \int_{V^e}\left(dF_{Vr}\vec{e}_r \cdot \frac{\partial u_r}{\partial q_j^e}\vec{e}_r\right)$$
$$= \int_0^{2\pi}\int_{A^e}\rho\Omega^2 r\sum_{m=0}^{N}\left(\frac{\partial U_{mrS}}{\partial q_j^e}\cos(m\theta) + \frac{\partial U_{mrA}}{\partial q_j^e}\sin(m\theta)\right)dAd\theta$$

(14)

where dF_{Vr} is centrifugal forces per unit volume and can be expressed as $dF_{Vr} = \rho\Omega^2 r$. q_j^e is the jth node DOF of the element. U_{mrS} and U_{mrA} are defined in Eq. (1). It can be seen from Eq. (14) that the integral over the circumferential angle $\theta = 0 \sim 2\pi$ eliminates the first- and second-order harmonics. That said, only the zeroth harmonics contribute to the initial stress and strain caused by centrifugal forces.

Applying the Lagrange's equations to the strain energy caused by centrifugal forces yields

$$\frac{\partial U_0^e}{\partial q_j^e} = Q_{Vj}^e \quad \text{with } U_0^e = \frac{1}{2}\int_V \{\varepsilon_0^e\}^T\{\sigma_0^e\}dV \tag{15}$$

where U_0^e represents the elastic strain energy of the element caused by centrifugal forces prior to the bending of the rotor. σ_0^e and ε_0^e are initial stress and strain caused by centrifugal forces, respectively. The node displacements induced by centrifugal forces $\{U_R^e\}$ can be solved based on Eq. (15). For isotropic homogeneous elastic materials, the initial stress $\{\sigma_0^e\}$ can be obtained from

$$\{\sigma_0^e\} = [D][\partial]\{U_R^e\} \tag{16}$$

where the linear stress–strain constitutive matrix $[D]$ and partial derivative matrix $[\partial]$ can be found in Ref. [11].

Substituting Eqs. (12) and (16) in Eq. (13) yields the strain energy due to centrifugal forces U_σ^e as

$$U_\sigma^e = \frac{1}{2}\int_{V_e}\{\delta_\sigma^e\}^T[S_\sigma^e]\{\delta_\sigma^e\}dV \tag{17}$$

where $[S_\sigma^e]$ represents the centrifugal stress matrix. $\{\delta_\sigma^e\}$ is the expanded strain vector derived from Eq. (12) by rearranging the second-order strain terms. Both are specified in the Appendix. By using the shape functions and node DOF shown in Eq. (2), U_σ^e can be further rearranged as

$$U_\sigma^e = \sum_{m=0}^{N}\frac{1}{2}\{q_m^e\}^T\left(\int_{V_e}[G_{\sigma m}^e]^T[S_\sigma^e][G_{\sigma m}^e]dV\right)\{q_m^e\} \tag{18}$$

Applying Lagrange's equations to Eq. (18) yields the elemental centrifugal stress-stiffening matrix for the mth harmonics $[K_{\sigma m}^e]$ as

$$\frac{\partial U_\sigma^e}{\partial \{q_m^e\}} = [K_{\sigma m}^e] = \int_{V_e}[G_{\sigma m}^e]^T[S_{\sigma 0}^e][G_{\sigma m}^e]dV \tag{19}$$

where $\{q_m^e\}$ represents the DOF vector for the mth harmonics. The total DOFs q_j^e contain the DOF for all harmonics and thereby include $\{q_m^e\}$. $[K_{\sigma m}^e]$ is given in the Appendix. Although only the zeroth modes contribute to the initial centrifugal stress, the strain energy due to centrifugal forces for the bending rotor is contributed by all harmonics. $[K_{\sigma m}^e]$ is the final centrifugal stress-stiffening matrix that will be used in the equation of motion for the axisymmetric solid element model.

Spin-Softening. In addition to the stress-stiffening effects, rotor spin induces so-called spin-softening effects. The effects are most pronounced for flexible disks or large-diameter, thin-walled shafts. Prior publications [11,22] provided qualitative discussions of this phenomenon but did not develop a formal FE treatment for the spin-softening effects utilizing axisymmetric elements.

Consider an axisymmetric element in a rotor. The additional body force ΔF_r results from the extension of the element beyond the initial element radius (distance between the element and the centerline of the rotor), which is caused by centrifugal forces. However, unlike the centrifugal forces discussed in Eq. (14), ΔF_r is independent of the element radius r. This can be explained by

$$F_r = \Omega^2\int_{V^e}\rho(r + u_r)dV \Rightarrow \Delta F_r = \Omega^2\int_{V^e}\rho u_r dV \tag{20}$$

where u_r is the radial displacement of the element with respect to the axis of symmetry. Then, the generalized external load Q_S^e may be written as

$$Q_{Sj}^e = \int_{V_e}d(\Delta F_r)\vec{e}_r \cdot \frac{\partial u_r}{\partial q_j^e}\vec{e}_r = \int_0^{2\pi}\int_{A^e}\rho\Omega^2 u_r\frac{\partial u_r}{\partial q_j^e}dAd\theta \tag{21}$$

where the subscript j indicates jth node DOF of the element.

Applying Eqs. (1) and (2) into Eq. (21) and further applying Lagrange's equations yields the elemental spin-softening matrix for the mth harmonics $[K_{\Omega m}^e]$ as

$$[K_{\Omega m}^e] = \frac{\partial \{Q_S^e\}}{\partial \{q_m^e\}} = \int_{V_e}[N_m]^T\begin{bmatrix} \rho\Omega^2 & 0 & 0 \\ 0 & 0 & 0 \\ 0 & 0 & 0 \end{bmatrix}[N_m]dV \tag{22}$$

Extra attention needs to be given to the zeroth harmonics that have a different formulation. $[K_{\Omega m}^e]$ is given in the Appendix.

Model Reduction. A solid element model may involve thousands of DOFs more than a beam element model. Thus, a reduction technique is desirable to obtain a solution within practical computer time limits. The Guyan reduction method [27] has been successfully applied to the shaft axisymmetric FE model in Ref. [10]. The master DOFs for this reduction technique are selected in such a way that the DOFs with large damping, inertia, or external load are retained [24].

To verify the effectiveness of the Guyan reduction method in terms of natural frequency prediction, the reduction technique is applied to a three-disk rotor without bearing support at the two
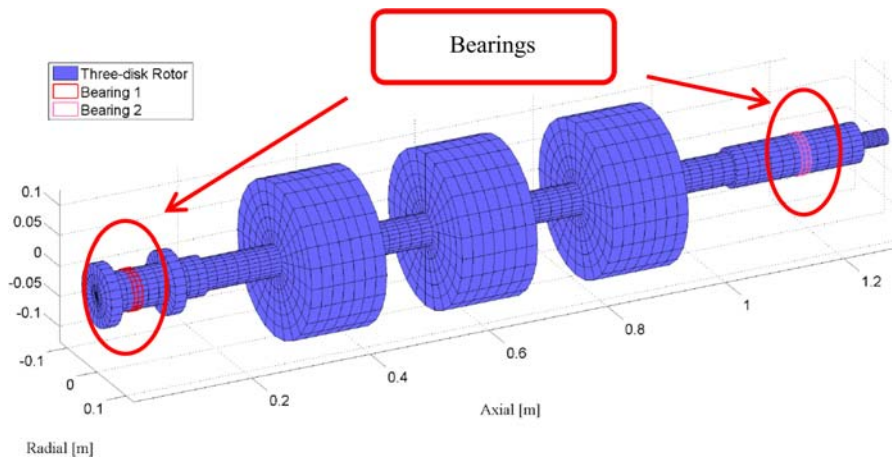
Fig. 6 Revolved axisymmetric solid element model of a three-disk rotor with two tilting-pad bearings support

ends (the same rotor as shown in Fig. 6 with bearings excluded). The master DOF selection algorithm presented in Ref. [28] is utilized to select retained degrees-of-freedom. This algorithm computes Q_i for each DOF, where $Q_i = K_{ii}/M_{ii}$, and K_{ii} and M_{ii} denote the ith main diagonal term of the stiffness and mass matrices, respectively. The quantity Q_i is used to determine whether the inertia terms are small. The algorithm tends to retain small Q_i.

The natural frequencies of the three-disk rotor at the spin speed of 0 rpm are compared between the unreduced and reduced axisymmetric FE models. The comparison results are illustrated in Table 1. The reduction levels are listed in the first row. The difference percentages between the unreduced and reduced models are given in the brackets. The measured natural frequencies obtained from Ref. [29] are included in the brackets of the second column. The retained DOF ratio is the ratio of the retained DOF number to the unreduced/original DOF number. According to the master DOF selection algorithm, the DOF with the smallest Q_i will be retained. It can be concluded from Table 1 that (a) Guyan reduction method is sufficiently accurate in terms of natural frequency prediction and (b) the accuracy decreases with higher modes.

To fairly compare axisymmetric solid and beam element models, however, the Guyan reduction method was not applied in the following comparison.

Simulation Results

The axisymmetric FE formulation derived above and in the Appendix is implemented in the rotor dynamics code. Before using the improved axisymmetric FE model for simulation, measured data for a three-disk rotor with two tilting-pad bearings support [30] is used to validate the rotor dynamics code. First, the

rotor is discretized with beam elements in the same way as shown in Table 2 of Ref. [30]. Then, an improved axisymmetric solid element rotor model is constructed as shown in Fig. 6 (axisymmetric element semi-section of the rotor revolves into a 3D rotor model).

As Table 2 illustrates, the natural frequency differences between the axisymmetric element model and measured data for the lowest five modes of the rotor system operating at 4000 rpm are no more than 5.1%. The results obtained from the axisymmetric FE model is more accurate than from the beam FE model for all modes except for the third mode. As pointed out in Ref. [30], the large differences between the FE model and the measurement are caused by the neglecting of foundation structure effects. Overall, the improved axisymmetric FE model presented in this work is verified to be sufficiently accurate for the following comparisons with the beam element model.

A variety of simulation cases are presented in the following sections to compare beam FE and axisymmetric solid FE rotor models and develop guidelines for appropriate selection of one or the other for specific applications.

Bearing Attachment. As mentioned in the previous bearing attachment section, excessive local distortions may occur if the bearing linear dynamic force coefficients (stiffness and damping) are not connected to the axisymmetric elements model in a manner that distributes the bearing forces. To illustrate this, consider the case of a cylindrical thin-walled shaft with $L/D_O = 4$ and $t = 0.025 D_O$ (refer to Table 3 for definitions). As shown in Fig. 7, the flexible shaft is supported by two identical symmetric bearings. The bearing damping is set to zero. The bearing stiffness is set as $K_{yy} = K_{zz} = 5K_S$ (i.e., stiff bearing), where $(K_S = 48EI/L^3)$ is

Table 1 Free-free natural frequencies of the non-rotating three-disk utilizing the master DOF selection algorithm and measured data obtained from Ref. [29]

Retained DOF ratio	100%	50%	25%	10%	5%	2%
Running time of a desktop with 3.7 GHz Intel Xeon CPU (min)	277.14	41.65	10.30	4.75	4.30	4.04
Natural freq. for 1st bending mode (Hz)	94.73 (measured = 94)	94.73 (+0.00%)	94.74 (+0.00%)	94.74 (+0.00%)	94.74 (0.01%)	97.74 (+0.01%)
Natural freq. for 2nd bending mode (Hz)	208.36 (measured = 207)	208.36 (+0.00%)	208.36 (+0.00%)	208.38 (+0.01%)	208.41 (+0.03%)	208.43 (+0.03%)
Natural freq. for 3rd bending mode (Hz)	357.63 (measured = 356)	357.65 (+0.00%)	357.66 (+0.01%)	357.75 (+0.03%)	357.92 (+0.08%)	357.98 (+0.10%)
Natural freq. for 4th bending mode (Hz)	463.05 (measured = 463)	463.07 (+0.00%)	463.11 (+0.01%)	463.46 (+0.09%)	464.02 (+0.21%)	464.19 (+0.25%)

Table 2 Comparison between beam element and axisymmetric solid element models of a three-disk rotor with two tilting-pad bearings support, operating at the spin speed of 4000 rpm

Natural frequency	Measured data from Ref. [29] (Hz)	Beam element (Hz)	Axisymmetric solid element (Hz)
ω_1 (backward)	N/A	30.79	29.62
ω_2 (forward)	31.25	32.95 (+5.4%)	31.64 (+1.2%)
ω_3 (backward and forward)	110.0	106.24 (−3.4%)	104.35 (−5.1%)
ω_4 (backward and forward)	125.0	132.11 (+5.7%)	127.10 (+1.7%)
ω_5 (forward)	N/A	139.59	139.01

Table 3 Parameters of axisymmetric and beam FE rotor models

Variable	Definition
L/D_O	Ratio of the straight shaft length to the shaft outer diameter, refer to Fig. 7
t/D_O	Ratio of the shaft wall thickness to the shaft outer diameter, refer to Fig. 7
L_d/D_O	Ratio of the disk thickness to the straight shaft outer diameter, refer to Fig. 15 for L_d
θ	Taper angle of the conical segment of a shaft, refer to Fig. 11 for θ
t/D_{Or}	Ratio of conical segment wall thickness to shaft outer diameter at the right end, refer to Fig. 11 for D_{Or}
K_B/K_S	Ratio of the bearing stiffness to the structural stiffness of the shaft, refer to the cylindrical thin-walled shaft section for K_B and K_S
1 or 2	The number of disks and their locations
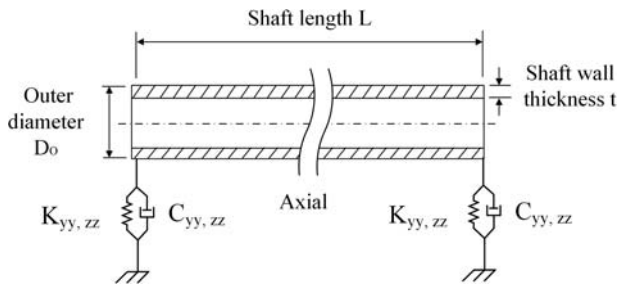
Fig. 7 Straight hollow shaft supported by two bearings

defined as the bending stiffness of a simply supported shaft with a central load.

Figure 8(a) shows modal deformations with the bearing coefficients applied at a single surface node, leading to excessive local distortions of the journal. Figure 8(b) shows the same mode shape with the bearing attachment made in a distributed manner as described in the bearing attachment section. "Distributed" here implies that each bearing stiffness coefficient is equally (or adjustable) divided by the same number of surface nodes of the journal and then attached to the surface nodes. This may help to eliminate unrealistic local deformations and warping.

Parameter Studies. The present paper identifies specific design features of a rotor system that is likely to cause inaccurate natural frequency predictions when using the beam FE model. Table 3 provides a list of related rotor parameters.

Cylindrical Thin-Walled Shaft. As depicted in Fig. 7, a dimensionless straight hollow shaft is supported by two identical bearings
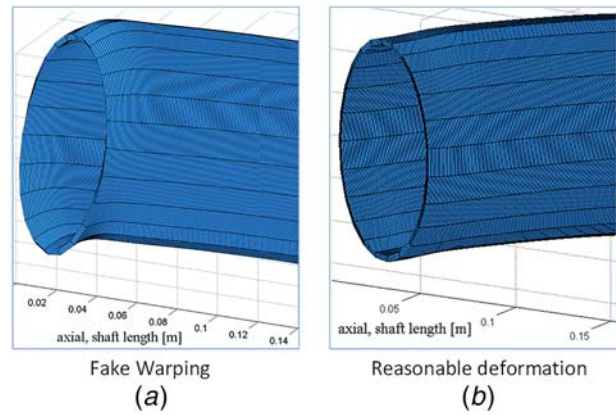

Fig. 8 Modal deformation of a thin-walled journal with stiff bearing supports: (a) point bearing attachment and (b) distributed bearing attachment
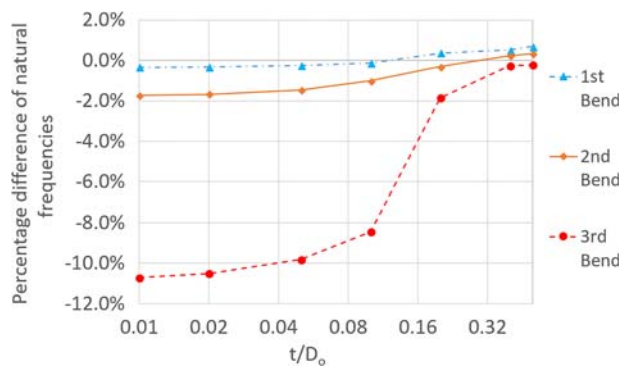

Fig. 9 Percentage difference of natural frequencies between axisymmetric and beam FE models for a free-free straight thin-walled shaft with $L/D_O = 4$

with symmetric stiffness (i.e., $K_{xx} = K_{yy} = K_B$) and zero damping. Various combinations of L/D_O, t/D_O, and K_B/K_S (K_S has been defined in the bearing attachment section of the simulation results chapter) have been investigated, and simulation results are demonstrated in Figs. 9 and 10. As can be seen from Fig. 9, the difference of free-free natural frequencies between solid and beam FE models becomes larger as shaft wall thickness gets thinner (i.e., t/D_O decreases). When $t/D_O = 0.04$, the difference exceeds 10%. The dimensionless natural frequency $\hat{\omega}_n$ is defined as

$$\hat{\omega}_n = \omega_n \sqrt{\frac{M_S}{K_S}} \quad \text{with } M_S = \frac{\rho\pi}{4}(D_O^2 - D_I^2)L \tag{23}$$

where ω_n is the natural frequency of the shaft.

Varying the bearing stiffness coefficients from 0.1 to 5 times the bending stiffness of the shaft with a central load shows the impact of bearing parameters on the prediction difference between axisymmetric FE and beam FE models. As can be seen from Fig. 10, the higher the bearing stiffness (i.e., K_B/K_S increases), the larger the difference. In addition, a shorter shaft (i.e., L/D_O shown in the upper figures of Fig. 10 are smaller than in the lower figures) or a thinner shaft wall (i.e., t/D_O shown in the left figures of Fig. 10 are smaller than in the right figures) also results in a larger prediction difference of natural frequencies.

Stepped, Thin-Walled Shaft. This section investigates a thin-walled shaft composed of both straight and conical/stepped segments. The conical/stepped segment is modeled with conical beam elements [7]. As Fig. 11 shows, the shaft is divided into
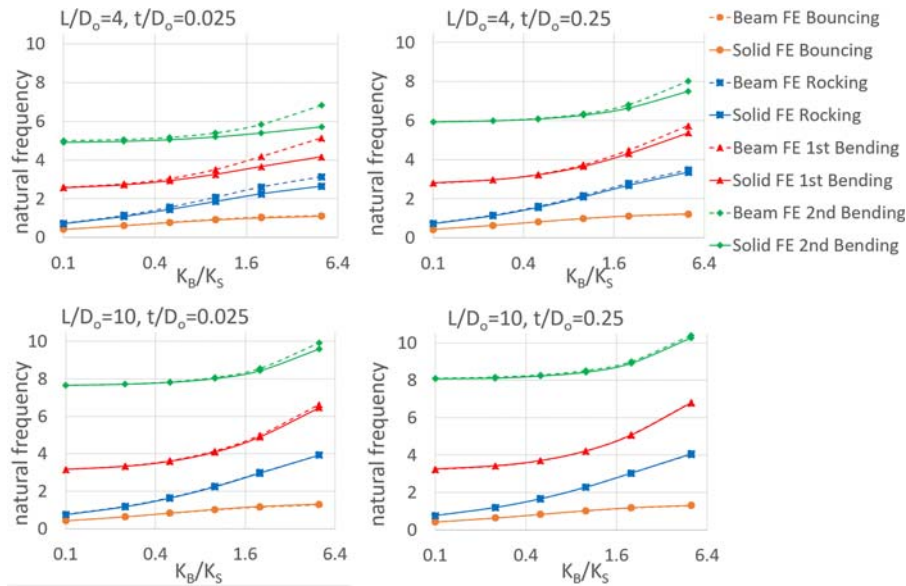
Fig. 10 Dimensionless natural frequencies of the straight thin-walled shaft supported by two bearings with four different rotor configurations
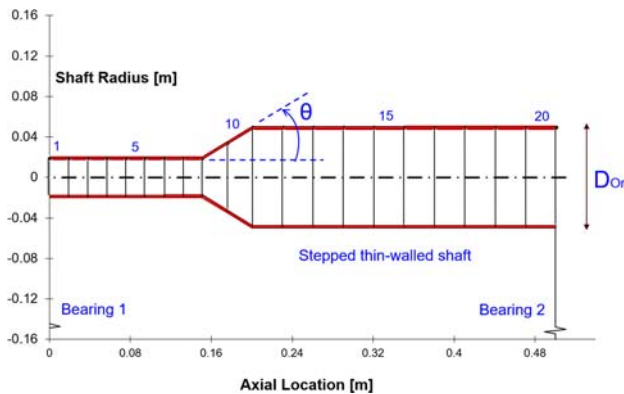

Fig. 11 Beam element model for a stepped thin-walled shaft

20 elements (the conical shaft segment generally consists of two elements, but the purely stepped shaft segment consists of one element and the conical segment with $\theta = 11$ deg consists of five elements). A variety of thin-walled shafts with $t/D_{Or} = 0.025$ and the gradually decreasing taper angles from 90 to 11 deg have been modeled with axisymmetric FEs, which are illustrated in Fig. 12.

Figure 13 shows the percentage difference variation of the first bending rotor mode versus taper angle, for the stepped diameter rotor. The percentage difference is defined as the ratio of the natural frequency difference between the beam element and axisymmetric element models to the natural frequency of the axisymmetric element model. It can be seen from the simulation results shown in Fig. 13 that as the taper angle gets smaller, the natural frequencies for the first bending mode predicted by the axisymmetric FE model become closer to those predicted by the beam FE model. As shown in Fig. 14, clearly non-beam deformations occur at the step location in the axisymmetric FE model, indicating that it may be inaccurate to use beam elements to model a stepped thin-walled shaft.

Thin-Walled Shaft With Flexible Disks. For a beam FE rotor model, a disk is typically represented by a rigid body with concentrated mass and inertia. However, its flexibility may become important as it gets relatively thin in comparison with the shaft diameter. Furthermore, if the first flexural modes of the disk appear within the operating speed range, the disk should not be treated as a rigid body.

A rotor system composed of a thin-walled shaft and a flexible disk is utilized to investigate the influences of a disk flexibility on natural frequencies. The corresponding 2D triangle mesh of the longitudinal section of the rotor is shown in Fig. 15 (the bottom semi-section is added just for visualization). The disk diameter is set as four times the outer diameter of the shaft. The stiffness of the two bearings that support the shaft at both ends varies from 0.1 to 5 times the bending stiffness of the shaft with a central load K_S (the same definition as in the bearing attachment section of the simulation results chapter). The other nondimensional constants that characterize the model include L/D_O, t/D_O, and L_d/D_O.

Simulation results are presented in Fig. 16, which show increasing difference between axisymmetric FE and beam FE model natural frequency predictions in the rocking mode as either the bearings get stiffer (i.e., K_B/K_S increases) or the shaft wall gets thinner (i.e., t/D_O shown in the left figures of Fig. 16 are smaller than in the right figures). This results from the greater amount of shaft deformation occurring as the bearings become stiffer and the wall thickness becomes smaller, which also affects the amount of shaft out of plane cross-sectional warping.

For illustration, consider comparing the natural frequency differences between the axisymmetric FE and beam FE model predictions at $K_B/K_S = 5$ (i.e., stiff bearing). As is shown in Fig. 16, the percentage difference decreases only by 4.9% in the rocking mode when just the shaft wall thickness ratio t/D_O is increased from 0.05 to 0.2, and the disk is relatively thick with $L_d/D_O = 0.5$. In contrast, the percentage difference rises significantly by 55.8% with a decrease in the disk thickness L_d/D_O from 0.5 to 0.2. This indicates that in the rocking mode disk thickness changes contribute more to the natural frequency difference than shaft wall thickness changes do. The thicker disk has only a slight effect on the difference in the bouncing and first bending modes. This results from the cross sections near the mid-span deforming heavily in the rocking mode while only slightly in the other two modes, which can be seen from Fig. 17. Additionally, an axisymmetric FE model can predict the first disk diametral mode while a beam FE model cannot.

The next example considers a rotor with two flexible disks and a thin-walled shaft. As shown in Fig. 18, the shaft length is set as $L/D_O = 15$, and the disk diameter is four times the outer diameter of the shaft. Two disks are installed at 1/4 and 3/4 length along the shaft. The variables considered are shaft wall thickness, disk thickness, and bearing stiffness. The lowest three mode shapes and their labels are provided in Fig. 19.
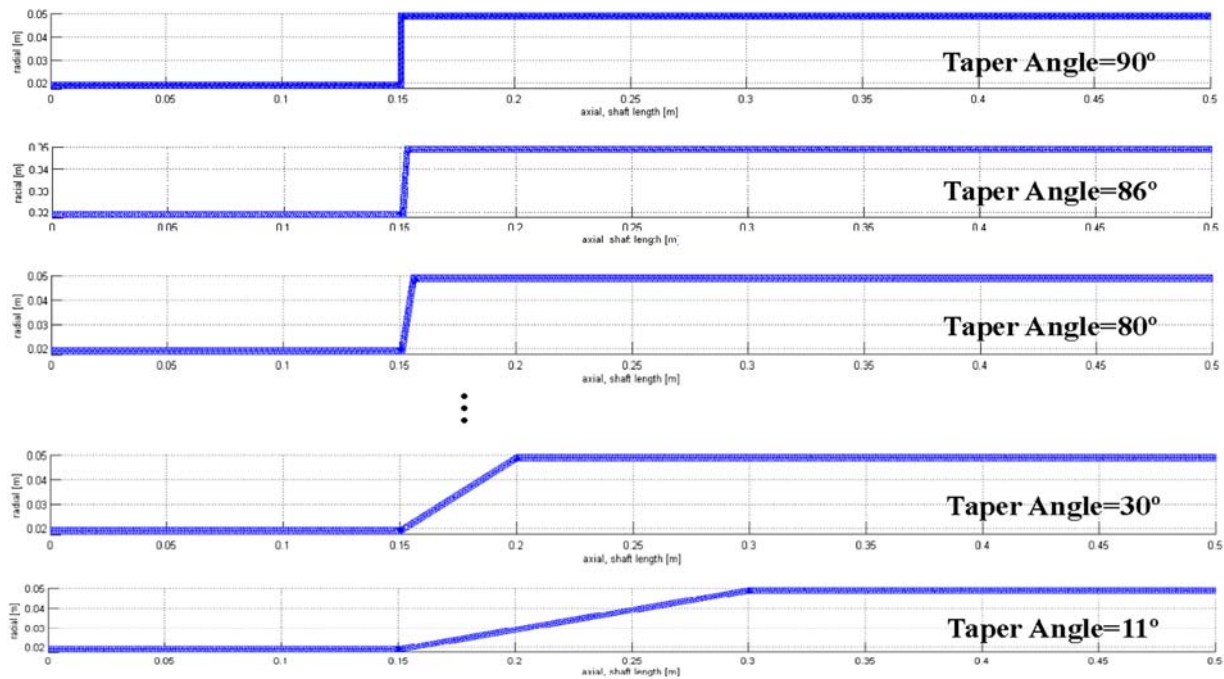
Fig. 12 Axisymmetric element models of longitudinal semi-sections of the step shafts with different taper angles
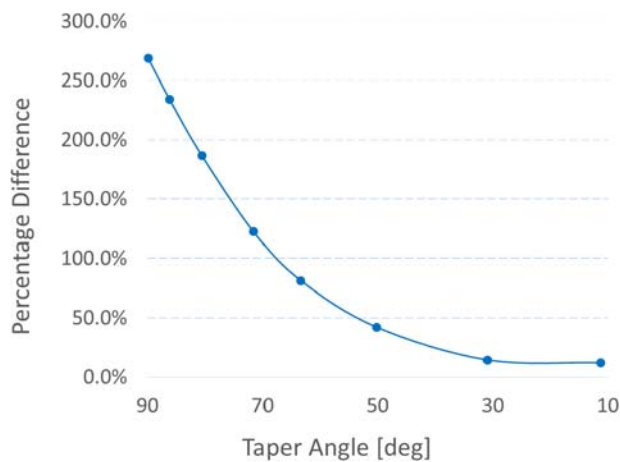

Fig. 13 Percentage difference of natural frequencies for the first bending mode between axisymmetric FE and beam FE models for a free-free step-like thin-walled shaft
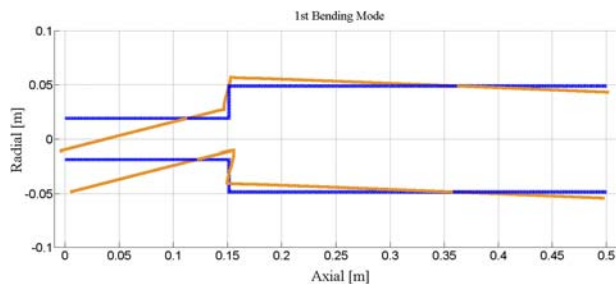

Fig. 14 Non-beam-like deformations of the solid element's longitudinal section of the step shaft in the first bending mode

Fig. 15 Longitudinal section mesh of a thin-walled shaft with a disk, shown here with $L/D_O = 8$, $t/D_O = 0.05$, and $L_d/D_O = 0.2$
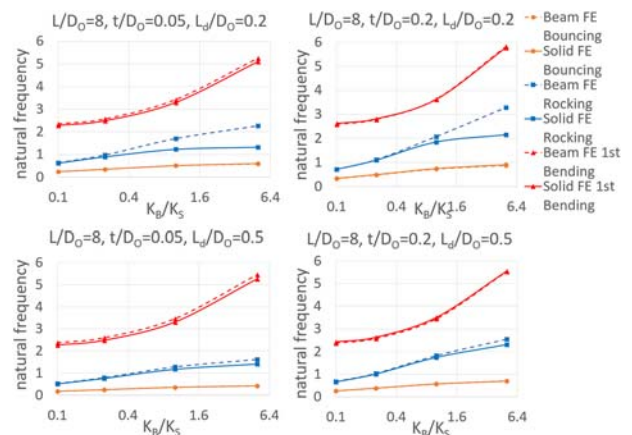

Fig. 16 Dimensionless natural frequencies of a thin-walled shaft with a disk supported by two bearings with four different rotor configurations

Figure 20 shows that for both bouncing and rocking modes, the predictions by the axisymmetric FE model are close to those by the beam FE model. This result can be explained the same way as in the straight thin-walled shaft case, i.e., the long shaft design with $L/D_O = 15$ helps reduce the difference. Nevertheless,

non-beam-like deformations increase in the first bending mode as the bearings get stiffer (i.e., K_B/K_S increases). A decrease in the thickness of the shaft wall, i.e., t/D_O shown in the upper left figure of Fig. 20 are smaller than in the upper right figure, or the disk, i.e., L_d/D_O shown in the upper left figure of Fig. 20 are
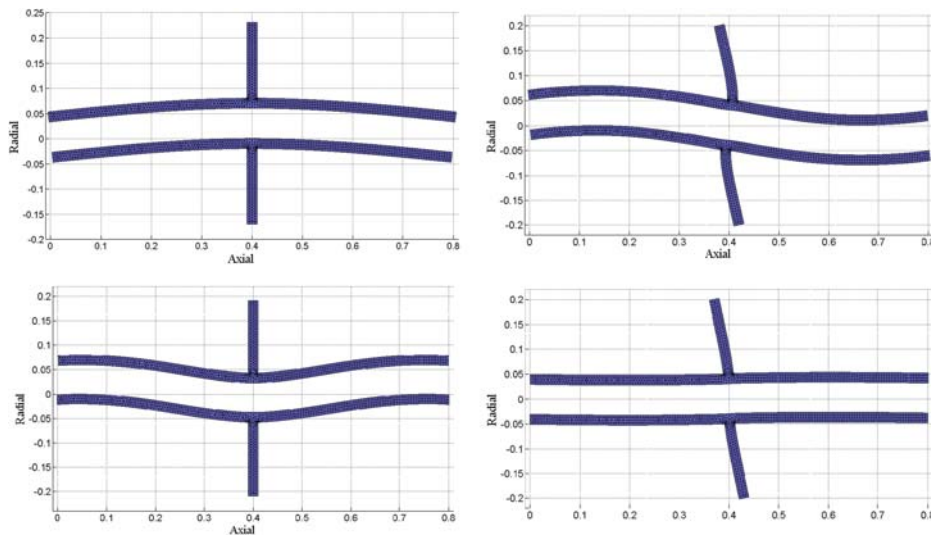
Fig. 17   Lowest four modes of a hollow shaft with a disk supported by two stiff bearings: $L/D_O = 8$, $t/D_O = 0.2$, $L_d/D_O = 0.2$, shaft bouncing mode (top left), shaft rocking mode (top right), the first shaft bending mode (bottom left), and the first disk diametral mode (bottom right)
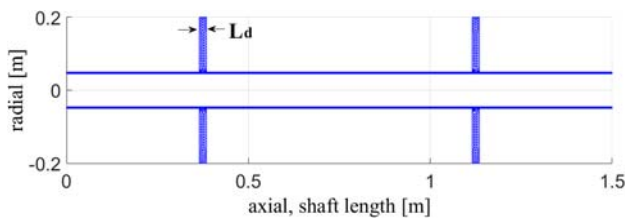

Fig. 18   Longitudinal section mesh of a thin-walled shaft with two disks: $L/D_O = 15$, $t/D_O = 0.05$, $L_d/D_O = 0.2$

smaller than in the lower left figure, may cause severer non-beam-like deformations. As a result, the difference between the axisymmetric FE and beam FE models rises even with a long shaft. However, the difference may be not apparent when either the shaft or the disk is thick, i.e., $t/D_O = 0.2$ or $L_d/D_O = 0.5$, which can be seen from the other figures of Fig. 20.

Summary and Conclusions

An axisymmetric solid element approach with improved modeling capabilities for flexible rotor systems has been presented along with illustrative numerical examples and parametric studies. Improvements include the centrifugal stress-stiffening and spin-softening effects. More accurate simulations of thin-walled shaft and flexible disk rotor dynamic response can be attained by using the improved axisymmetric elements.

The implementation of the centrifugal stress-stiffening and spin-softening matrices enables an accurate prediction of the change of resonant frequencies and critical speeds caused by the rotation of the rotor.

Bearing forces are distributed to a number of nodes within the range of the longitudinal bearing length rather than a single surface node of the journal to prevent fictitious, excessive local distortions of the thin-walled journal.

Only the zeroth-, first-, and second-order harmonics are included in the axisymmetric FE model.

Both thin-walled shafts and flexible disks are prone to non-beam-like deformations. Natural frequency predictions using beam FE differs more from axisymmetric FE predictions when the shaft length gets shorter and wall gets thinner. Investigation of various thin-walled stepped shafts with straight and conical segments
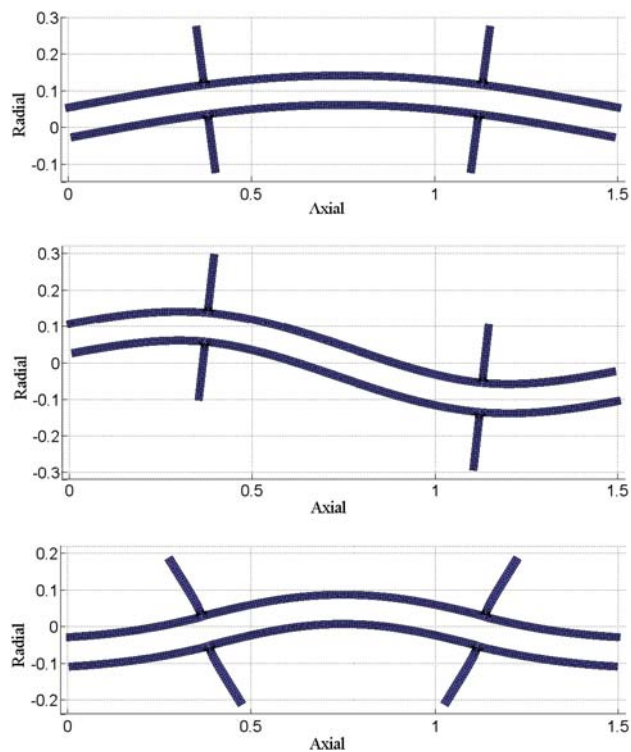

Fig. 19   Lowest three modes of a thin-walled shaft with two disks, supported by two stiff bearings: $L/D_O = 15$, $t/D_O = 0.2$, $L_d/D_O = 0.2$; shaft bouncing mode (top), shaft rocking mode (middle), and the first shaft bending mode (bottom)

shows that the difference between the axisymmetric FE and beam FE predicted natural frequencies becomes larger with the increase in the taper angle of the conical segment.

Disk flexibility and locations have an impact on the prediction accuracy of the beam FE model compared with the axisymmetric element model. If a thin disk, implying more flexibility, is installed at the mid-span of a thin-walled shaft, then a large prediction difference tends to occur at the rocking mode due to large deformations of the disk. In contrast, a large difference of predicted natural frequencies between the axisymmetric and beam
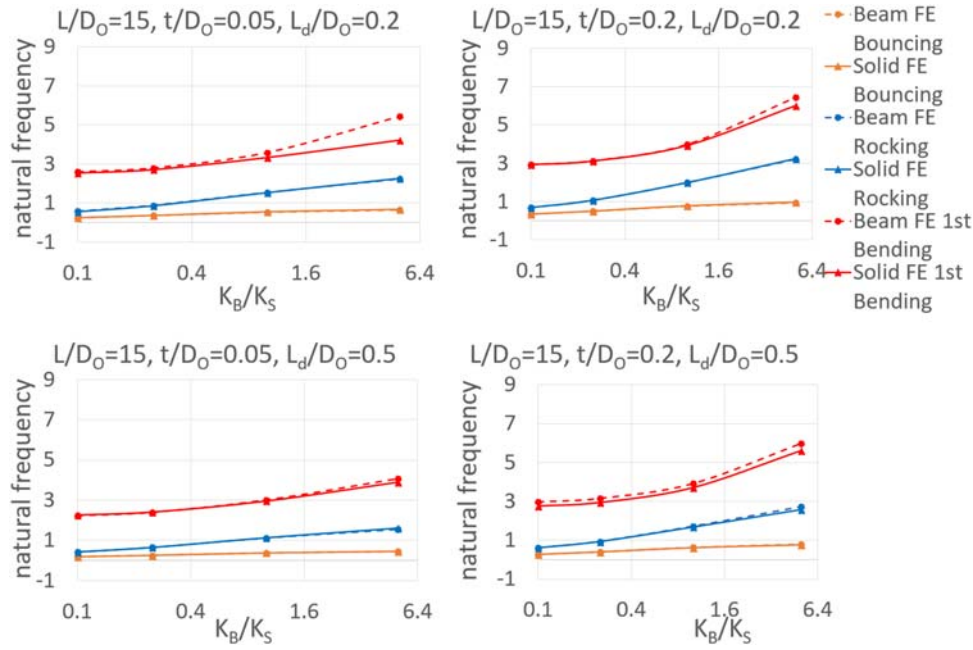
Fig. 20   Dimensionless natural frequencies of a thin-walled shaft with two disks supported by two bearings with four different rotor configurations

FE models may appear at the first bending mode if two flexible disks are symmetrically placed away from the center of the shaft at quarter spans.

The comparison results can be used for guidance on choosing the axisymmetric solid or the beam FE models in the rotor design and rotor dynamic analysis.

Future Work

As the shaft wall gets thinner, the axisymmetric FE mesh model needs refinement, which may require more computer resources. In this case, a shell element model could be a better choice in terms of computation efficiency. Thus, a thorough comparison of the axisymmetric FE model with the shell FE model should be conducted in order to understand the pros and cons of these two rotor modeling approaches. The centrifugal stress-stiffening and spin-softening matrices developed in the present work should be integrated into the axisymmetric FE model for the comparison.

Acknowledgment

Nomenclature

q = node degree-of-freedom
r = element radius with respect to the axis of symmetry
A = area
D = diameter of the shaft or disk
E = elastic modulus of the shaft
I = second moment of inertia of the shaft
V = bounded volume region
$\vec{e}$ = unit vector
$[\mathbf{N}]$ = shape function matrix
$\{\mathbf{U_R^e}\}$ = displacement vector of a rotor element
ρ = mass density
Ω = spin speed of the rotor
$()_{A,\,S}$ = antisymmetric or symmetric component
$()_{I,\,O}$ = inner or outer of the rotor
$()_{Or}$ = outer right end of the rotor
$()_R$ = rotor
$()_e$ = elemental
$()_m$ = mth harmonics
$()_{r,\,z,\,\theta}$ = radial, axial, or circumferential direction

Appendix

As shown in Eq. (10), the generalized bearing force acting on the circle of node P, Q_j^P, can be expressed as

(a) when the DOF q_j corresponds to U_{nrS}^P shown in Eq. (1) with $n = 0, 1, 2 \ldots$

$$
\begin{aligned}
Q_j^P = & -\left\{ K_{yy} \sum_{m=0}^{N} u_{mrS}^P + K_{yz} \left[\sum_{m=0,\,2,\,\ldots}^{N} u_{mrS}^P \cdot (-1)^{m/2} + \sum_{m=1,\,3,\,\ldots}^{N} u_{mrA}^P \cdot (-1)^{(m-1)/2} \right] \right\} \\
& - \left\{ K_{zz} \left[\sum_{m=0,\,2,\,\ldots}^{N} u_{mrS}^P \cdot (-1)^{m/2} + \sum_{m=1,\,3,\,\ldots}^{N} u_{mrA}^P \cdot (-1)^{(m-1)/2} \right] + K_{zy} \sum_{m=0}^{N} u_{mrS}^P \right\} \cdot \begin{cases} 0, & \text{if } n \text{ is odd} \\ (-1)^{n/2}, & \text{if } n \text{ is even} \end{cases}
\end{aligned}
$$

(A1)

(b) when the DOF q_j corresponds to U_{nrA}^P shown in Eq. (1) with $n = 0, 1, 2\ldots$

$$Q_j^P = -\left\{ K_{zz}\left[\sum_{m=0, 2, \ldots}^{N} u_{mrS}^P \cdot (-1)^{m/2} + \sum_{m=1, 3, \ldots}^{N} u_{mrA}^P \cdot (-1)^{(m-1)/2}\right] + K_{zy}\sum_{m=0}^{N} u_{mrS}^P \right\} \cdot \begin{cases} 0, & \text{if } n \text{ is even} \\ (-1)^{(n-1)/2}, & \text{if } n \text{ is odd} \end{cases} \tag{A2}$$

The above equations are applicable even if the harmonics number m exceeds 2.
The expanded strain vector $\{\boldsymbol{\delta_\sigma^e}\}$ shown in Eq. (17) is written as

$$\{\boldsymbol{\delta_\sigma^e}\} = \left[\frac{\partial u_r}{\partial r}, \frac{\partial u_r}{\partial z}, \frac{1}{r}\left(\frac{\partial u_r}{\partial \theta} - u_\theta\right), \frac{\partial u_z}{\partial r}, \frac{\partial u_z}{\partial z}, \frac{1}{r}\frac{\partial u_z}{\partial \theta}, \frac{\partial u_\theta}{\partial r}, \frac{\partial u_\theta}{\partial z}, \frac{1}{r}\left(u_r + \frac{\partial u_\theta}{\partial \theta}\right)\right]^T \tag{A3}$$

As the elemental centrifugal stress-stiffening matrix shown in Eq. (19) can be further expressed as

$$[\mathbf{K_{\sigma m}^e}] = \pi\int_{A_e} ([\mathbf{G_{\sigma mc}^e}]^T[\mathbf{S_{\sigma 0}^e}][\mathbf{G_{\sigma mc}^e}] + [\mathbf{G_{\sigma ms}^e}]^T[\mathbf{S_{\sigma 0}^e}][\mathbf{G_{\sigma ms}^e}])r\,dr\,dz \tag{A4}$$

where

$$[\mathbf{S_\sigma^e}] = \begin{bmatrix} [\boldsymbol{\sigma_0^e}] & [\mathbf{0}] & [\mathbf{0}] \\ [\mathbf{0}] & [\boldsymbol{\sigma_0^e}] & [\mathbf{0}] \\ [\mathbf{0}] & [\mathbf{0}] & [\boldsymbol{\sigma_0^e}] \end{bmatrix} \tag{A5}$$

$$\left[\mathbf{G_{\sigma mc}^e}\right]_{9\times 18} = \begin{bmatrix} 0 & 0 & 0 & & & 0 & 0 & 0 & & \\ \frac{\partial N_{m1}}{\partial z} & 0 & 0 & \cdots & \cdots & 0 & 0 & 0 & \cdots & \cdots \\ 0 & 0 & 0 & & & \frac{mN_{m1}}{r} & 0 & \frac{N_{m1}}{r} & & \\ 0 & \frac{\partial N_{m1}}{\partial r} & 0 & & & 0 & 0 & 0 & & \\ 0 & 0 & 0 & 2* & 3* & 0 & 0 & 0 & 2* & 3* \\ 0 & 0 & 0 & & & 0 & \frac{mN_{m1}}{r} & 0 & & \\ 0 & 0 & 0 & & & 0 & 0 & -\frac{\partial N_{m1}}{\partial r} & & \\ 0 & 0 & 0 & \cdots & \cdots & 0 & 0 & -\frac{\partial N_{m1}}{\partial z} & \cdots & \cdots \\ 0 & 0 & 0 & & & 0 & 0 & 0 & & \end{bmatrix} \tag{A6}$$

$$\left[\mathbf{G_{\sigma ms}^e}\right]_{9\times 18} = \begin{bmatrix} 0 & 0 & 0 & & & 0 & 0 & 0 & & \\ 0 & 0 & 0 & \cdots & \cdots & \frac{\partial N_{m1}}{\partial z} & 0 & 0 & \cdots & \cdots \\ -\frac{mN_{m1}}{r} & 0 & -\frac{N_{m1}}{r} & & & 0 & 0 & 0 & & \\ 0 & 0 & 0 & & & 0 & \frac{\partial N_{m1}}{\partial r} & 0 & & \\ 0 & 0 & 0 & 2* & 3* & 0 & 0 & 0 & 2* & 3* \\ 0 & -\frac{mN_{m1}}{r} & 0 & & & 0 & 0 & 0 & & \\ 0 & 0 & \frac{\partial N_{m1}}{\partial r} & & & 0 & 0 & 0 & & \\ 0 & 0 & \frac{\partial N_{m1}}{\partial z} & \cdots & \cdots & 0 & 0 & 0 & \cdots & \cdots \\ 0 & 0 & 0 & & & 0 & 0 & 0 & & \end{bmatrix} \tag{A7}$$

where 2* indicates that these three columns have the same form as the left three columns next to them except that the shape function terms N_{m1} are replaced by N_{m2}, and a similar convention for 3*.

As shown in Eq. (22), the elemental spin-softening matrix for the mth harmonics ($m \neq 0$) may be rearranged as

$$\left[K_{\Omega m}^e\right]_{18\times 18} = \begin{bmatrix} \left[K_{\Omega mS}\right]_{9\times 9} & [0]_{9\times 9} \\ [0]_{9\times 9} & \left[K_{\Omega mS}\right]_{9\times 9} \end{bmatrix} \tag{A8}$$

where

$$
\left[K^e_{\Omega mS} \right]_{9\times 9} = \Omega^2 \rho \int_{A_e}
\begin{bmatrix}
N_{m1}N_{mj} & 0 & 0 \\
0 & 0 & 0 \\
0 & 0 & N_{m1}N_{mj} \\
\hline
N_{m2}N_{mj} & 0 & 0 \\
0 & 0 & 0 \\
0 & 0 & N_{m2}N_{mj} \\
\hline
N_{m3}N_{mj} & 0 & 0 \\
0 & 0 & 0 \\
0 & 0 & N_{m3}N_{mj}
\end{bmatrix}
\begin{array}{|c|c}
 & \\
 j = 2 & j = 3 \\
 &
\end{array}
\; r\,dr\,dz
\tag{A9}
$$

where $j = 2$ indicates that the three columns have the same form as the left three columns next to them except that the shape function terms N_{m1} are replaced by N_{m2}, and a similar convention for $j = 3$.

$[\mathbf{K}^{\mathbf{e}}_{\mathbf{\Omega m}}]$ for the zeroth harmonics is different than Eqs. (A8) and (A9). When $m = 0$, $[\mathbf{K}^{\mathbf{e}}_{\mathbf{\Omega m}}]$ may be written as

$$
\left[K^e_{\Omega 0} \right]_{18\times 18} =
\begin{bmatrix}
\left[K_{\Omega 0S} \right]_{9\times 9} & \left[0 \right]_{9\times 9} \\
\left[0 \right]_{9\times 9} & \left[K_{\Omega 0A} \right]_{9\times 9}
\end{bmatrix}
\tag{A10}
$$

where

$$
\left[K^e_{\Omega 0S} \right]_{9\times 9} = \Omega^2 \rho \int_{A_e}
\begin{bmatrix}
N_{01}N_{0j} & 0 & 0 \\
0 & 0 & 0 \\
0 & 0 & 0 \\
\hline
N_{02}N_{0j} & 0 & 0 \\
0 & 0 & 0 \\
0 & 0 & 0 \\
\hline
N_{03}N_{0j} & 0 & 0 \\
0 & 0 & 0 \\
0 & 0 & 0
\end{bmatrix}
\begin{array}{|c|c}
 & \\
 j = 2 & j = 3 \\
 &
\end{array}
\; r\,dr\,dz
\tag{A11}
$$

$$
\left[K^e_{\Omega 0A} \right]_{9\times 9} = \Omega^2 \rho \int_{A_e}
\begin{bmatrix}
0 & 0 & 0 \\
0 & 0 & 0 \\
0 & 0 & N_{01}N_{0j} \\
\hline
0 & 0 & 0 \\
0 & 0 & 0 \\
0 & 0 & N_{02}N_{0j} \\
\hline
0 & 0 & 0 \\
0 & 0 & 0 \\
0 & 0 & N_{03}N_{0j}
\end{bmatrix}
\begin{array}{|c|c}
 & \\
 j = 2 & j = 3 \\
 &
\end{array}
\; r\,dr\,dz
\tag{A12}
$$

where the convention for $j = 2, 3$ is similar to Eq. (A9).

References

[1] Myklestad, N. O., 1944, "A New Method of Calculating Natural Modes of Uncoupled Bending Vibration of Airplane Wings and Other Types of Beams," J. Aeronaut. Sci. **11**(2), pp. 153–162.

[2] Pestel, E., and Leckie, F., 1963, *Matrix Methods in Elasto Mechanics*, McGraw-Hill, New York.

[3] Nelson, H. D., and McVaugh, J. M., 1976, "The Dynamics of Rotor-Bearing Systems Using Finite Elements," ASME J. Eng. Ind., **98**(2), pp. 593–600.

[4] Nelson, H. D., 1980, "A Finite Rotating Shaft Element Using Timoshenko Beam Theory," ASME J. Mech. Des., **102**(4), pp. 793–803.

[5] Thomas, D. L., Wilson, J. M., and Wilson, R. R., 1973, "Timoshenko Beam Finite Elements," J. Sound Vib., **31**(3), pp. 315–330.

[6] Rouch, K. E., and Kao, J. S., 1979, "A Tapered Beam Finite Element for Rotor Dynamics Analysis," J. Sound Vib., **66**(1), pp. 119–140.

[7] Greenhill, L. M., Bickford, W. B., and Nelson, H. D., 1985, "A Conical Beam Finite Element for Rotor Dynamics Analysis," ASME J. Vib. Acoust. Stress Reliab. Des., **107**(4), pp. 421–430.

[8] Stephenson, R. W., Rouch, K. E., and Arora, R., 1989, "Modelling of Rotors with Axisymmetric Solid Harmonic Elements," J. Sound Vib., **131**(3), pp. 431–443.

[9] Vest, T. A., and Darlow, M. S., 1990, "A Modified Conical Beam Element Based on Finite Element Analysis: Experimental Correlations," ASME J. Vib. Acoust., **112**(3), pp. 350–354.

[10] Stephenson, R. W., and Rouch, K. E., 1993, "Modeling Rotating Shafts Using Axisymmetric Solid Finite Elements With Matrix Reduction," ASME J. Vib. Acoust., **115**(4), pp. 484–489.

[11] Cook, R. D., Malkus, D. S., Plesha, M. E., and Witt, R. J., 2001, *Concepts and Applications of Finite Element Analysis*, Wiley, New York.

[12] Geradin, M., and Kill, N., 1984, "A New Approach to Finite Element Modelling of Flexible Rotors," Eng. Comput., **1**(1), pp. 52–64.

[13] Genta, G., and Tonoli, A., 1996, "A Harmonic Finite Element for the Analysis of Flexural, Torsional and Axial Rotordynamic Behaviour of Discs," J. Sound Vib., **196**(1), pp. 19–43.

[14] Genta, G., and Tonoli, A., 1997, "A Harmonic Finite Element for the Analysis of Flexural, Torsional and Axial Rotordynamic Behavior of Blade Arrays," J. Sound Vib., **207**(5), pp. 693–720.

[15] Greenhill, L. M., and Lease, V. J., 2007, "Additional Investigations Into the Natural Frequencies and Critical Speeds of a Rotating, Flexible Shaft-Disk System," ASME Paper No. GT2007-28065, pp. 995–1003.

[16] Genta, G., 2005, *Dynamics of Rotating Systems*, Springer, New York.

[17] Genta, G., 2011, "Dynamic Modeling of Rotors: A Modal Approach," *IUTAM Symposium on Emerging Trends in Rotor Dynamics*, Vol. 1011, K. Gupta, ed., Springer, Dordrecht.

[18] Datta, A., 2016, "X3D—A 3D Solid Finite Element Multibody Dynamic Analysis for Rotorcraft," American Helicopter Society Technical Meeting on Aeromechanics Design for Vertical Lift, Francisco, CA, Jan. 20–22.

[19] Tseng, C.-W., Shen, J.-Y., Kim, H., and Shen, I. Y., 2005, "A Unified Approach to Analyze Vibration of Axisymmetric Rotating Structures With Flexible Stationary Parts," ASME J. Vib. Acoust., **127**(2), pp. 125–138.

[20] Kiesel, T., and Marburg, S., 2016, "Simulation of Mode-Locking Phenomena in a Complex Nonlinear Rotor System Using 3D Solid Finite Elements," Proc. Inst. Mech. Eng. C, **230**(6), pp. 959–973.

[21] Hu, L., and Palazzolo, A., 2016, "Solid Element Rotordynamic Modeling of a Rotor on a Flexible Support Structure Utilizing Multiple-Input and Multiple-Output Support Transfer Functions," ASME J. Eng. Gas Turbines Power, **139**(1), p. 012503.

[22] Combescure, D., and Lazarus, A., 2008, "Refined Finite Element Modelling for the Vibration Analysis of Large Rotating Machines: Application to the Gas Turbine Modular Helium Reactor Power Conversion Unit," J. Sound Vib., **318**(4–5), pp. 1262–1280.

[23] Zienkiewicz, O. C., Taylor, R. L., and Zhu, J. Z., 2005, *The Finite Element Method: Its Basis and Fundamentals*, Butterworth-Heinemann, Boston.

[24] Palazzolo, A., 2016, *Vibration Theory and Applications with Finite Elements and Active Vibration Control*, Wiley, UK.

[25] Suh, J., and Palazzolo, A., 2014, "Three-Dimensional Thermohydrodynamic Morton Effect Simulation—Part I: Theoretical Model," ASME J. Tribol., **136**(3), p. 031706.

[26] Suh, J., and Palazzolo, A., 2014, "Three-Dimensional Thermohydrodynamic Morton Effect Analysis—Part II: Parametric Studies," ASME J. Tribol., **136**(3), p. 031707.

[27] Guyan, R. J., 1965, "Reduction of Stiffness and Mass Matrices," AIAA J., **3**(2), pp. 380–380.

[28] Kohnke, P. C., 1989, "ANSYS Engineering Analysis System Theoretical Manual," Swanson Analysis System, Inc., Houston, PA.

[29] Vance, J. M., Murphy, B. T., and Tripp, H. A., 1987, "Critical Speeds of Turbomachinery: Computer Predictions vs. Experimental Measurements—Part I: The Rotor Mass-Elastic Model," ASME J. Vib. Acoust. Stress Reliab. Des., **109**(1), pp. 1–7.

[30] Vance, J. M., Murphy, B. T., and Tripp, H. A., 1987, "Critical Speeds of Turbomachinery: Computer Predictions vs. Experimental Measurements—Part II: Effect of Tilt-Pad Bearings and Foundation Dynamics," ASME J. Vib. Acoust. Stress Reliab. Des., **109**(1), pp. 8–14.